

Intraseasonal Variability of the West African Monsoon and Atlantic ITCZ

ERIC D. MALONEY AND JEFFREY SHAMAN

College of Oceanic and Atmospheric Sciences, Oregon State University, Corvallis, Oregon

(Manuscript received 18 April 2007, in final form 1 October 2007)

ABSTRACT

Intraseasonal variability of boreal summer rainfall and winds in tropical West Africa and the east Atlantic is examined using daily Tropical Rainfall Measuring Mission (TRMM) precipitation and the NCEP–NCAR reanalysis during 1998–2006. Intraseasonal precipitation variability is dominated by two significant spectral peaks at time scales near 15 and 50 days, accompanied by corresponding peaks in eddy kinetic energy (EKE) and eddy enstrophy. Regional precipitation variability on 30–90-day time scales is significantly correlated (+0.6) with a global Madden–Julian oscillation time series based on equatorial zonal winds, supporting the results of A. J. Matthews. The overall amplitude of the 30–90-day West African monsoon precipitation variability during a given summer, however, does not appear to be strongly regulated by interannual variability in MJO amplitude.

Composite analysis and complex empirical orthogonal function analysis shows that 30–90-day precipitation anomalies are generally zonally elongated, grow and decay in place, and have maximum amplitude near the Gulf of Guinea and in the Atlantic ITCZ. Composite 30–90-day enhanced precipitation events are accompanied by a significant suppression of eastern North Atlantic trade winds. Suppressed 30–90-day precipitation events are associated with an enhancement of the Atlantic trade winds. Enhanced (suppressed) EKE occurs just to the north of the east Atlantic ITCZ during positive (negative) 30–90-day precipitation events, with the maximum EKE magnitude lagging precipitation events by about 5 days.

East Atlantic tropical cyclone activity is significantly modulated on intraseasonal time scales. The number of tropical cyclones that occur in the Atlantic's main development region to the east of 60°W is suppressed about 5–10 days before maxima in a regional intraseasonal precipitation time series, and enhanced about 5–10 days after time series maxima. An analysis of east Atlantic tropical cyclone activity based on an equatorial MJO index produces similar results. Consistent with the results of K. C. Mo, variations in vertical shear may help explain this modulation of tropical cyclone activity.

1. Introduction

Tropical West Africa and the eastern Atlantic are characterized by complex interactions across many time and space scales during boreal summer (e.g., Redelsperger et al. 2002; Nicholson and Grist 2003; Redelsperger et al. 2006). Intraseasonal variability of the West African monsoon has received increased attention of late and was a significant motivation for the recent African Monsoon Multidisciplinary Analysis (AMMA; Redelsperger et al. 2006). Boreal summer variations in rainfall and winds over tropical and subtropical West Africa and adjacent regions of the Atlan-

tic appear to be dominated by two distinct time scales of 10–25 days and 25–60 days (e.g., Janicot and Sultan 2001; Sultan et al. 2003; Mounier et al. 2008). Intraseasonal variability on 10–25-day time scales has been more thoroughly documented than that at longer time scales. Rainy periods associated with 10–25-day variability are accompanied by an enhancement of moist low-level southwesterly flow into sub-Saharan Africa and an enhancement of African easterly wave activity (Sultan and Janicot 2003). The meridional isentropic potential vorticity (IPV) gradient in West Africa appears to exhibit fluctuations on 10–25-day times that may be related to variations in African easterly wave activity (e.g., Lavaysse et al. 2006).

Examination of boreal summer West African monsoon variability at time scales of greater than 25 days has been more limited. Although time scales of 10–25 days are thought to dominate West African monsoon

Corresponding author address: Eric D. Maloney, Department of Atmospheric Science, Colorado State University, 1371 Campus Delivery, Fort Collins, CO 80523-1371.
E-mail: emaloney@atmos.colostate.edu

variations (e.g., Sultan et al. 2003), previous studies note that substantial intraseasonal monsoon variability occurs at time scales of greater than 25 days (Janicot and Sultan 2001; Sultan et al. 2003). Gu and Adler (2004) recently used Tropical Rainfall Measuring Mission (TRMM) precipitation to show that a distinct 25–50-day peak in eastward-propagating variability at zonal wavenumbers 1–5 can be found in the West African monsoon region during boreal summer.

The impact of global modes of intraseasonal variability on boreal summer West African monsoon rainfall and winds is less understood. An example of such a mode of variability is the Madden–Julian oscillation (MJO; e.g., Madden and Julian 2005), characterized by 30–90-day time scales. Foltz and McPhaden (2004) found a significant modulation of Atlantic trade winds by the MJO through comparison to an outgoing long-wave radiation (OLR)-based MJO index. However, the MJO influence was not stratified by season, and overall intraseasonal variability in surface winds peaked during boreal winter in association with the North Atlantic Oscillation. Matthews (2004) documented 20–200-day variability in winds and convection over the eastern Atlantic and sub-Saharan Africa during boreal summer, and he suggested a connection to the global MJO. Matthews showed that OLR anomalies associated with the leading 20–200-day mode of variability over tropical West Africa and the east Atlantic are zonally elongated and modulate the strength of convection at the mean position of the intertropical convergence zone (ITCZ). Equatorial Kelvin waves induced by the MJO in the Pacific may initiate West African convection, which then locally amplifies through interactions with the large-scale circulation (similar to the east Pacific amplification mechanism described by Maloney and Esbensen 2003). Matthews (2004) also suggested that the MJO may alter the IPV gradient over sub-Saharan Africa, making African easterly wave (AEW) formation more favorable there during periods of enhanced monsoonal low-level westerly flow and precipitation. Reversal of the IPV gradient over West Africa produces conditions favorable for the growth of AEWs through combined barotropic and baroclinic instability (Thorncroft and Hoskins 1994a,b). A modeling study by Thorncroft and Rowell (1998) suggests that understanding AEW activity in a given season is tantamount to understanding intraseasonal variability of the IPV gradient over sub-Saharan Africa.

It should be stressed that the influence of the MJO on wind, precipitation, and AEWs over the African monsoon region remains unclear. The influence of the MJO on sub-Saharan Africa has been found to be weak in many studies (e.g., Knutson and Weickmann 1987;

Annamalai and Slingo 2001; Wheeler and Weickmann 2001) and almost nonexistent in others (e.g., Knutson et al. 1986; Murakami et al. 1986; Maloney and Hartmann 2000a). However, Matthews's (2004) work suggests that strong MJO events can have a remote influence on the African monsoon region and modulate precipitation, winds, and AEW activity there. If the West African monsoon is influenced by coherent global modes of intraseasonal variability such as the MJO, skillful subseasonal forecasts for this region may be realized, which may have important consequences because the Sahel is a source of easterly waves that can spawn tropical cyclones (TCs; e.g., Landsea et al. 1998; Vintzileos and Thiaw 2006).

Modulation of Atlantic tropical cyclones by the MJO has been previously examined by Maloney and Hartmann (2000b) and Mo (2000). Maloney and Hartmann (2000b) showed a significant MJO-related modulation of tropical cyclones in the western part of the Atlantic, including the Gulf of Mexico and the Caribbean Sea. Hurricanes were 4 times more likely to occur during certain phases of the MJO than others. Mo (2000) analyzed a larger portion of the Atlantic basin and found a significant modulation of TC activity by the MJO. Primary emphasis was placed on the area to the west of 60°W, where TC activity varied with the first principal component of Eastern Hemisphere OLR used to define the MJO. Mo (2000) cited vertical shear variations as one possible explanation for this modulation of tropical cyclone activity. Vertical shear has been found by many previous studies to be a factor in tropical cyclogenesis potential (e.g., Shapiro 1987; Gray 1998; Camargo et al. 2007).

In this paper, we examine intraseasonal variability of the West African monsoon, with emphasis on 30–90-day time-scale variability, time scales typically associated with the MJO. We use satellite-based daily mean Tropical Rainfall Measuring Mission precipitation data to examine the spatial structure of 30–90-day variations of precipitation during boreal summer. This work is motivated in part by the analysis of Gu and Adler (2004), who examined the spectral characteristics of West African and the Atlantic ITCZ intraseasonal variability using TRMM precipitation, although these authors did not examine the spatial structure of such variability. Our analysis of the spatial structure of precipitation variability also includes a complex empirical orthogonal function analysis, which succinctly captures the propagation characteristics of such variability. Gu and Adler (2004) also did not explicitly examine the relationship of such variability to global modes of variability. We will test the contention of Matthews (2004) that the MJO significantly impacts boreal summer vari-

ability in the West African monsoon region, through explicitly relating West African precipitation variability to a global MJO index derived by Maloney and Hartmann (1998). Our analysis also examines how tropical synoptic eddy and cyclone activity varies with 30–90-day oscillations of the West African monsoon. This analysis will concentrate on the east Atlantic ITCZ region between 60°W and the African coast, an area that was noted but received relatively little emphasis in the investigations of Mo (2000) and Maloney and Hartmann (2000b). In general, our work builds on previous work related to 30–90-day variability of the West African monsoon by using improved datasets and by employing new and/or expanded analyses that provide further insight into the intraseasonal variability of this region.

Section 2 describes the datasets used in this study. Section 3 briefly describes the general characteristics of intraseasonal variability in the West African monsoon region, as well as the spectral characteristics of intraseasonal precipitation. Section 3 also examines the relationship of regional 30–90-day precipitation variability to the MJO. Section 4 describes the spatial structure of boreal summer 30–90-day wind, precipitation, and eddy kinetic energy anomalies in the Atlantic ITCZ and West Africa. Section 5 describes the modulation of east Atlantic TC activity on 30–90-day time scales. Section 6 presents conclusions and discussion.

2. Data

We use daily mean precipitation fields during June–October of 1998–2006 from the TRMM 3B42, version 6, product, incorporating several satellite measurements including the TRMM Microwave Imager (TMI) and TRMM precipitation radar to calibrate infrared precipitation estimates from geostationary satellites (e.g., Huffman et al. 2001). For calculation of spectra, an expanded May–October period is used to minimize bandwidth so that spectral peaks at intraseasonal time scales can be better resolved. May–October spectra are qualitatively consistent with those derived from the shorter June–October period, however. The precipitation data were downloaded from the Goddard Space Flight Center Distributed Access Archive System on a $0.25^\circ \times 0.25^\circ$ grid (accessed from <http://trmm.gsfc.nasa.gov/>). For more efficient analysis, precipitation data were first averaged to a $1^\circ \times 1^\circ$ grid, although sensitivity tests using a subset of the analyses described below show similar results for a $0.25^\circ \times 0.25^\circ$ grid. Nicholson et al. (2003) showed that the TRMM 3B42 product produces relatively small rainfall biases in West Africa during summertime relative to gauge data, at

least at monthly to seasonal time scales. Maloney and Esbensen (2007) used TRMM precipitation during 1998–2005 to examine the intraseasonal variability of east Pacific warm pool precipitation during boreal summer.

National Centers for Environmental Prediction (NCEP)–National Center for Atmospheric Research (NCAR) reanalysis I wind fields and related derived quantities such as eddy kinetic energy and eddy enstrophy were used from the surface to 100 hPa during 1998–2006 (Kalnay et al. 1996). Oceanic surface winds from NCEP reanalysis show general agreement to Quick Scatterometer (QuikSCAT) ocean vector winds (e.g., Chelton and Freilich 2005) during June–October of 2000–06 in the West African monsoon region when comparing seasonal mean winds and intraseasonal wind anomalies, although synoptic-scale eddy variance appears to be higher in QuikSCAT than in NCEP reanalysis. We note specific comparisons between QuikSCAT and NCEP winds below. NCEP reanalysis 850-hPa zonal winds were used for an extended period from 1979–2006 to develop an equatorial MJO index for use in comparison to West African and Atlantic intraseasonal variability.

We use the Atlantic hurricane best-track dataset from the National Hurricane Center (NHC)–Tropical Prediction Center (Jarvinen et al. 1984) to examine variations in Atlantic tropical cyclone activity to the east of 60°W during 1998–2006. The entire dataset extends back to 1851. Positions and intensities of Atlantic tropical cyclones are recorded 4 times daily at 0000, 0600, 1200, and 1800 UTC.

3. Variance and time series analysis

a. Mean and variance fields

Mean June–October precipitation is shown in Fig. 1a, indicating high mean precipitation in the ITCZ along 7°N in the Atlantic and general enhanced mean precipitation across most of western North Africa to the south of 16°N. A prominent precipitation maximum centered about 5°N, 8°E exists near the Gulf of Guinea.

Figure 1b shows June–October intraseasonal precipitation variance during 1998–2006. This plot shows total intraseasonal variance and does not select for certain intraseasonal periods through bandpass filtering. Total intraseasonal precipitation variance is defined as follows: 1) the seasonal cycle is constructed by averaging data on each calendar day over all 9 yr, and then smoothed using six passes of a 1–2–1 running filter (effectively a 9-day low-pass filter). This seasonal cycle is then removed from the raw precipitation data; 2) a low-

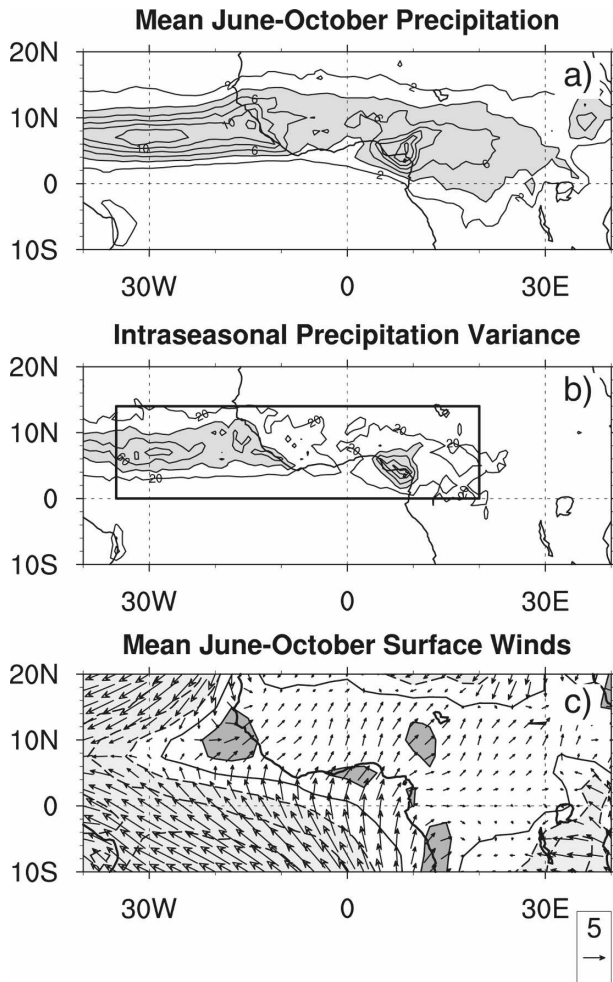


FIG. 1. June–October (a) mean precipitation, (b) intraseasonal precipitation variance, and (c) mean surface wind vectors and zonal wind. The contour interval in (a) is 2 mm day^{-1} , with values greater than 4 mm day^{-1} shaded. The contour interval in (b) is $20 \text{ mm}^2 \text{ day}^{-2}$, with values greater than $40 \text{ mm}^2 \text{ day}^{-2}$ shaded. The contour interval in (c) is 2 m s^{-1} , with values greater (less) than 2 m s^{-1} (-2 m s^{-1}) dark (light) shaded. The reference vector (m s^{-1}) is shown at the bottom right. The rectangle in (b) shows the averaging region used to define the regional precipitation time series.

pass filter with half-power point at 10 days is used to remove most synoptic-scale precipitation variability (e.g., African easterly waves); and 3) the mean over each individual June–October period is subtracted, effectively removing the impacts of interannual variability. Figure 1b shows that intraseasonal precipitation variance maximizes where mean precipitation is high, with strongest variance in the Gulf of Guinea and along the Atlantic ITCZ. Narrower frequency bands (e.g., 30–90 days) have qualitatively similar spatial distributions to that shown in Fig. 1b, although smaller magnitudes (not shown).

Figure 1c shows mean June–October surface winds from NCEP reanalysis during the period 1998–2006. As with other monsoonal regimes (e.g., east Pacific, Xie et al. 2005, Maloney and Esbensen 2007), the summertime low-level flow is characterized by cross-equatorial flow that transitions to mean low-level southwesterly flow to the north of the equator. The strongest mean southwesterly flow occurs in the Gulf of Guinea and along 10°N near the west coast of Africa in association with the Atlantic ITCZ. Grodsky et al. (2003) discuss this wind feature along the West African coast in detail, which takes the form of a low-level jet that can achieve a daily mean wind speed of 10 m s^{-1} during peak years.

b. Power spectra

Previous work has shown that the dominant modes of boreal summer intraseasonal variability at both 30–90-day and 10–25-day time scales are characterized by zonally extended structures with OLR anomalies of the same sign spanning West Africa and the eastern Atlantic (e.g., Matthews 2004; Mounier and Janicot 2004). These zonally extended modes are characteristic of modulation of the mean areas of precipitation. Taking advantage of the zonally extended nature of intraseasonal variability suggested by these previous studies, we analyze the spectral characteristics of TRMM precipitation averaged within a zonally extended box defined by $0^\circ\text{--}14^\circ\text{N}$, $35^\circ\text{W--}20^\circ\text{E}$, which spans West Africa and the Atlantic ITCZ and encompasses the region of heightened intraseasonal variance as shown in Fig. 1b. While such an averaging region likely excludes contributions of westward-propagating variability at smaller spatial scales ($\sim 6000\text{-km}$ wavelength) that are also observed in the West African monsoon (e.g., Mounier and Janicot 2004; Sultan et al. 2003), we will show (following) in a complex empirical orthogonal function (CEOF) analysis that the leading mode of variability at 30–90-day time scales appears to be characterized by the type of zonally extended structure that we select for here. We also feel that the larger averaging region employed here will generate more robust statistics than a smaller averaging region, given the short 9-yr precipitation record employed and the inherently noisy nature of tropical precipitation.

Before we calculated spectra for each of the nine May–October segments during 1998–2006, the seasonal cycle was removed. The seasonal cycle was computed by averaging fields on each calendar day of the year across all 9 yr of record, and then applying six passes of a 1–2–1 running filter (as described in association with Fig. 1b above). Results are not sensitive to the exact means by which the seasonal cycle is removed. Before calculation of each spectrum, the first and last 5% of

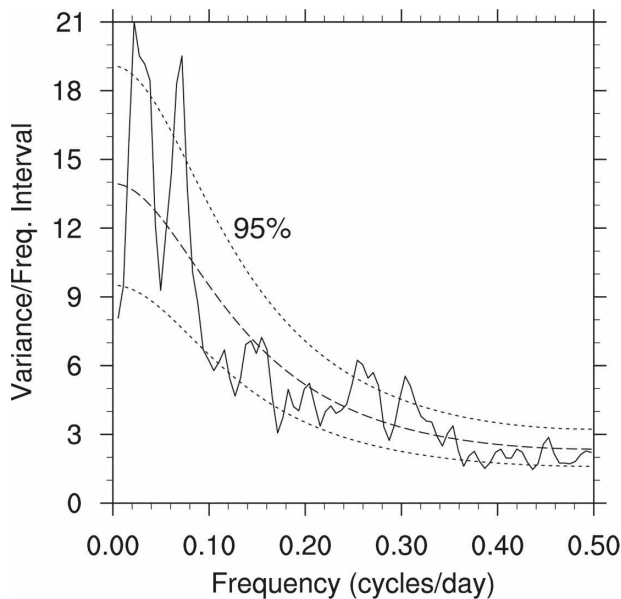


FIG. 2. Power spectrum of May–October TRMM precipitation averaged over the domain 0° – 14° N, 35° W– 20° E. The climatological seasonal cycle was removed before computation of the spectrum. Also shown are the red noise background spectrum and the 95% confidence limits on this background spectrum.

each May–October time series were tapered using a cosine bell functional form to reduce spurious sidelobes in the frequency response function, which are generated by the finite window length used to calculate the spectrum. Spectra are calculated on each individual May–October period and then averaged across all 9 yr of the record. Degrees of freedom are maximized by applying a 3-point Daniell smoother to the spectral estimates (essentially a 1–2–1 smoother), with the resulting spectral estimates each containing about 45 degrees of freedom. Smoothing results in more degrees of freedom per spectral estimate at the expense of effective bandwidth (e.g., Jenkins and Watts 1968). A red noise background spectrum is computed from the formula of Gilman et al. (1963), using the average of the 1-day and the square root of the 2-day lag autocorrelations; then the 95% confidence limits about this red noise spectrum are determined using the F statistic.

Figure 2 shows the average May–October precipitation spectrum for the 0° – 14° N, 35° W– 20° E averaging box described above and shown in Fig. 1b. Two significant spectral peaks for precipitation exist at intraseasonal time scales. One spectral peak is centered near a period of 15 days, and another peak is centered near a period of 50 days. The 15-day peak presumably corresponds to the strong 10–25-day monsoon variability extensively documented in previous studies (e.g., Janicot and Sultan 2001; Grodsky and Carton 2001). The Fig. 2

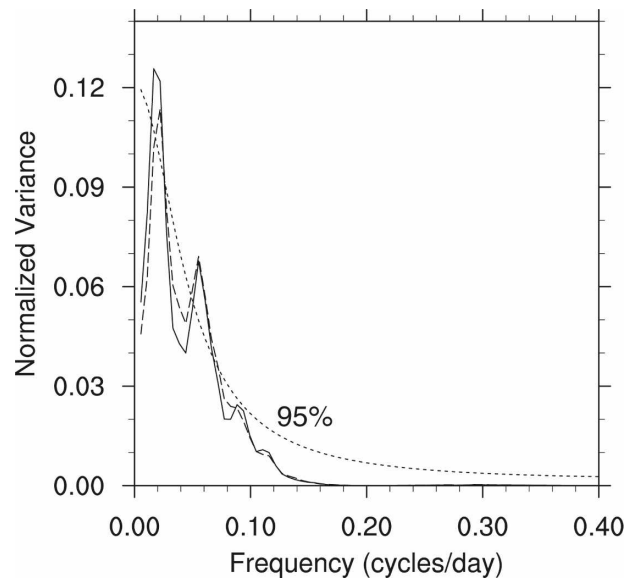


FIG. 3. Normalized power spectra of May–October EKE (solid) and EE (dashed) averaged over the domain 0° – 17.5° N, 40° W– 10° E. The climatological seasonal cycle was removed before computation of the spectrum. Also shown is the upper 95% confidence limit on the background red noise spectrum (not shown). The upper confidence limit is the same for both EKE and EE spectra because the average of the 1-day and the square root of the 2-day lag autocorrelations are the same for both.

spectrum also indicates significant spectral power at periods of 3–5 days, presumably in association with African easterly waves (e.g., Reed et al. 1977), although our zonally extended averaging domain is not optimal for analyzing such disturbances because they have zonal wavelengths of 2000–4000 km. We will be primarily concerned with longer time-scale precipitation variability centered near 50 days throughout the remainder of this paper. We note that the power spectrum of West African gauge rainfall presented by Sultan et al. (2003) shows similar spectral characteristics to those presented here, with prominent peaks near 15 days and 50 days.

Similar spectra are derived for surface eddy kinetic energy (EKE) and eddy enstrophy (EE). Eddy wind components u' and v' are defined as the deviation from the 5-day running mean of the surface zonal and meridional wind, respectively (effectively a 10-day high-pass filter). EE is computed as the 5-day average squared vorticity of these surface eddy wind components, and EKE is defined by the 5-day average of $u'^2 + v'^2$. For reasons to become apparent in section 4a in the composite analysis of 30–90-day EKE variations, we compute the spectrum of EE and EKE averaged over the domain 0° – 17.5° N, 40° W– 10° E. Figure 3 shows that as with precipitation, prominent EE and EKE spectral peaks occur near time scales of 15 days and 50

days. These spectral peaks for both EE and EKE are statistically significant at the 95% confidence level. As will be shown in sections 4a and 5, a statistically significant modulation of tropical synoptic scale variance and TC activity occurs during 30–90-day oscillations of precipitation and winds in the West African monsoon region. By definition, EE and EKE spectral variance becomes negligible below periods of 10 days.

c. Comparison with a global MJO time series

The rest of this paper will concentrate on 30–90-day variability of the West African monsoon and Atlantic ITCZ during boreal summer. This period band is selected because it brackets the 50-day spectral peaks shown in Figs. 2, 3. The results presented below are similar, if a somewhat wider frequency window is used (e.g., 25–100 days). We derive an index of 30–90-day West African precipitation variations during June–October by filtering TRMM precipitation during 1998–2006 with a linear nonrecursive digital filter with half-power points at 30 and 90 days, and then averaging the filtered precipitation field over the domain 0° – 14° N, 35° W– 20° E. This averaging region is shown in Fig. 1b. As will be shown below in the complex empirical orthogonal function analysis, this precipitation time series characterizes the leading mode of 30–90-day precipitation variability over the West African monsoon region during June–October. We will first compare this regional 30–90-day time series to a measure that characterizes the global evolution of the MJO, to confirm the hypothesis of Matthews (2004) that the MJO significantly modulates West African and east Atlantic wind and precipitation variability during boreal summer.

As described in Maloney and Hartmann (1998), and more recently in Maloney and Esbensen (2007), a global MJO time series can be derived by conducting an empirical orthogonal function (EOF) analysis on the 30–90-day bandpass-filtered 850-hPa equatorial (5° N– 5° S) zonal wind from NCEP reanalysis during 1979–2006. The leading two EOFs, explaining 59% of the variance, are a quadrature pair that maximize in amplitude over the Indian and western Pacific Oceans, respectively, and represent the eastward-propagating equatorial wind anomalies associated with the MJO. The principal component corresponding to EOF2 (PC2) lags PC1 by 12 days, and thus an MJO time series can be derived by adding PC1 to the value of PC2 12 days later. Our method is related to other methods of MJO index construction that use single-variable- and multivariate-method EOF analysis on equatorial fields (e.g., see the discussion in Wheeler and Hendon 2004).

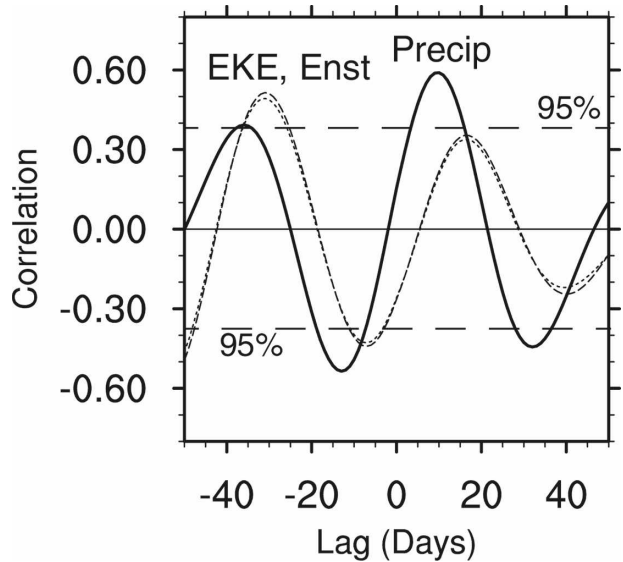


FIG. 4. June–October lag correlations of the MJO time series with the 30–90-day precipitation time series (solid) and the 30–90-day time series of EKE (dashed) and EE (dotted). Positive lags indicate that the MJO time series leads. Dashed horizontal lines indicate where correlations are significantly different from zero at the 95% confidence level.

We correlate the regional 30–90-day precipitation time series during June–October with the equatorial MJO time series as a function of time lag. The results of this analysis are shown in Fig. 4. The maximum correlation between the MJO index and the regional 30–90-day time series is +0.6, with the regional time series lagging the MJO index by about 10 days. This correlation is statistically significant at the 95% confidence level by conservatively assuming that each 50-day period represents an independent sample, for a total of 27 degrees of freedom during June–October across all 9 yr of the precipitation record. Using the t statistic with a two-tailed test, correlations with magnitude greater than 0.38 are statistically significant at the 95% confidence level, and such confidence limits are shown as horizontal dashed lines in Fig. 4. Given the method used to construct the MJO index, maxima in the index represent peak 850-hPa easterly anomalies in the equatorial Indian Ocean. Thus, the correlations of Fig. 4 are consistent with Matthews (2004, see his Fig. 5), who showed that 925-hPa easterly anomalies in the Indian Ocean lead minimum OLR in West Africa by about 10 days. The statistically significant correlation between the global MJO index and the regional-time TRMM precipitation series supports the hypothesis of Matthews (2004) that the MJO significantly modulates convective variability in West Africa and the eastern Atlantic during boreal summer. The MJO appears to

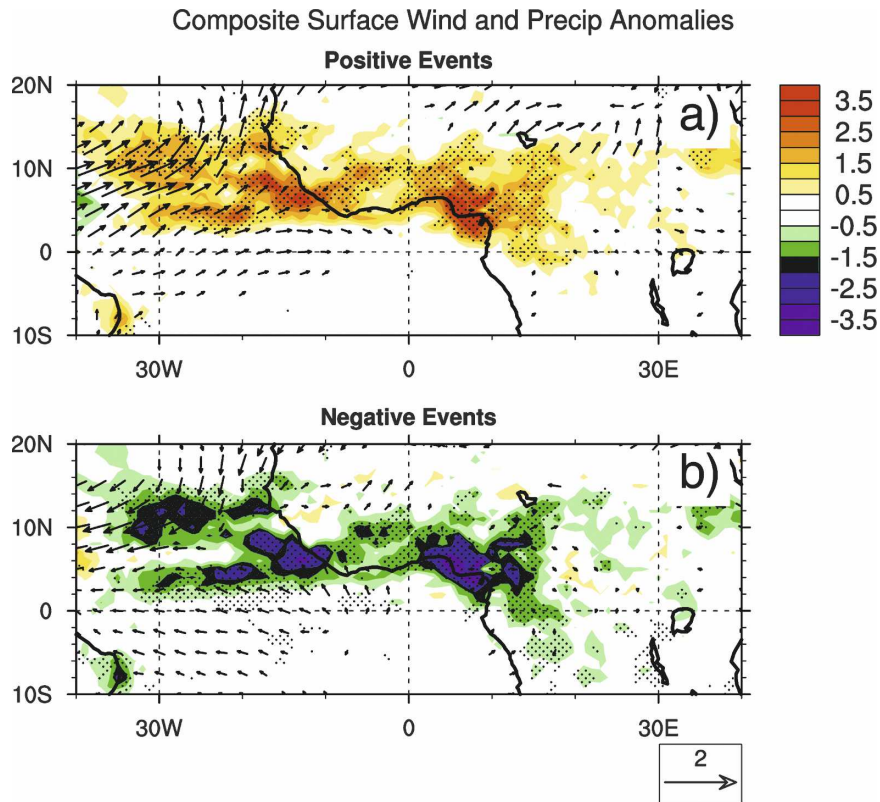


FIG. 5. Composite precipitation and surface wind anomalies for (a) positive and (b) negative 30–90-day precipitation events. Precipitation anomaly units are mm day^{-1} . The reference vector in m s^{-1} is shown at the bottom right. Stippling indicates where precipitation anomalies are significantly different from zero at the 95% confidence level. Only wind vectors significant at the 95% confidence level are shown.

explain about 1/3 of the 30–90-day precipitation variance in the West African monsoon region and Atlantic ITCZ during June–October.

June–October correlations between the global MJO index and regional 30–90-day bandpass-filtered EKE and EE (0° – 17.5°N , 40°W – 10°E averaged) were also examined (Fig. 4). While correlations are lower than with precipitation, the global MJO time series appears to be significantly correlated with the regional time series of 30–90-day EKE and EE. EKE and EE generally lag the precipitation time series by about 5 days. This relationship will be explored in more detail in the composites below.

4. Spatial structure of 30–90-day variability

a. Wind, precipitation, and eddy kinetic energy composites

To examine the spatial structure of 30–90-day variability in the West African monsoon region, we use strong deviations of the 30–90-day bandpass-filtered re-

gional precipitation time series to define events. Strong June–October extrema of the precipitation time series with magnitude greater than 1σ are selected, for a total of 15 positive precipitation events and 16 negative precipitation events. The σ is defined as the standard deviation of the regional precipitation time series during 1998–2006. Composites are generated by averaging precipitation and wind fields across all positive and negative events. Although we generate composites separately for positive and negative events, comparable results can be obtained by only using positive or negative deviations to define events, and then generating composite fields as a function of time lag.

Figure 5 shows composite surface wind and precipitation anomalies associated with positive and negative events. Only wind vectors statistically significant from zero at the 95% confidence level are shown. Also indicated are regions where composite precipitation anomalies are significantly different from zero at the 95% confidence level (stippling). Bandpass-filtered precipitation anomalies are approximately normally distributed about the composite mean. Statistical sig-

nificance was determined from the t statistic using a two-tailed test that incorporates the number of events along with the standard deviation about the composite mean. Positive (negative) events are characterized by a statistically significant enhancement (suppression) of precipitation along 8°N from West Africa into the eastern Atlantic. The latitude band of significant precipitation anomalies is slightly larger in the Atlantic. Strongest precipitation anomalies occur near the Gulf of Guinea and also in the Atlantic to the west of 10°W . Suppressed (enhanced) trade winds accompany enhanced (suppressed) precipitation over the Atlantic. Interestingly, the precipitation anomalies in the Gulf of Guinea are not accompanied by significant surface wind anomalies. To verify these reanalysis-derived surface fields, we recalculated composite fields using QuikSCAT ocean vector winds during 2000–06. Results were similar to those obtained here (not shown). The modulation of trade wind activity we observe on intraseasonal time scales resembles that in the OLR-based boreal summer analysis of Matthews (2004) and also resembles that found by Foltz and McPhaden (2004, 2005), although the Foltz and McPhaden analysis was dominated by boreal winter variability. Although the pattern of TRMM precipitation anomalies is similar to that of the OLR-based analysis of Matthews (2004), the localization of the strongest anomalies ($>13.5 \text{ mm day}^{-1}$) to the Gulf of Guinea and to the west coast of Africa near 15°W is even more striking than that found in Matthews (2004).

A sense of the vertical structure of 30–90-day wind anomalies can be gained by examining meridional cross sections. Figure 6 shows the vertical structure of mean June–October zonal wind and composite positive event zonal wind anomalies for a longitude band in the Atlantic ITCZ region (40° – 20°W averaged). Anomalies for negative precipitation events are similar, although of opposite sign. Stippling indicates where anomalies are significantly different from zero at the 95% confidence level. Zonal wind anomalies during the enhanced precipitation phase have a simple baroclinic structure in the vicinity of 10°N , with lower tropospheric westerly anomalies peaking between 700 and 850 hPa, and easterly anomalies in the upper troposphere. The main development region (MDR) for tropical cyclones in the Atlantic to the east of 60°W occurs between 10° and 20°N (e.g., Goldenberg and Shapiro 1996). Comparison of zonal wind anomalies to the mean zonal wind profile suggests that sizeable variations in vertical wind shear during 30–90-day precipitation events may be produced. Vertical shear has been shown to have deleterious impacts on tropical cyclone development and intensity (e.g., DeMaria 1996). How intraseasonal shear

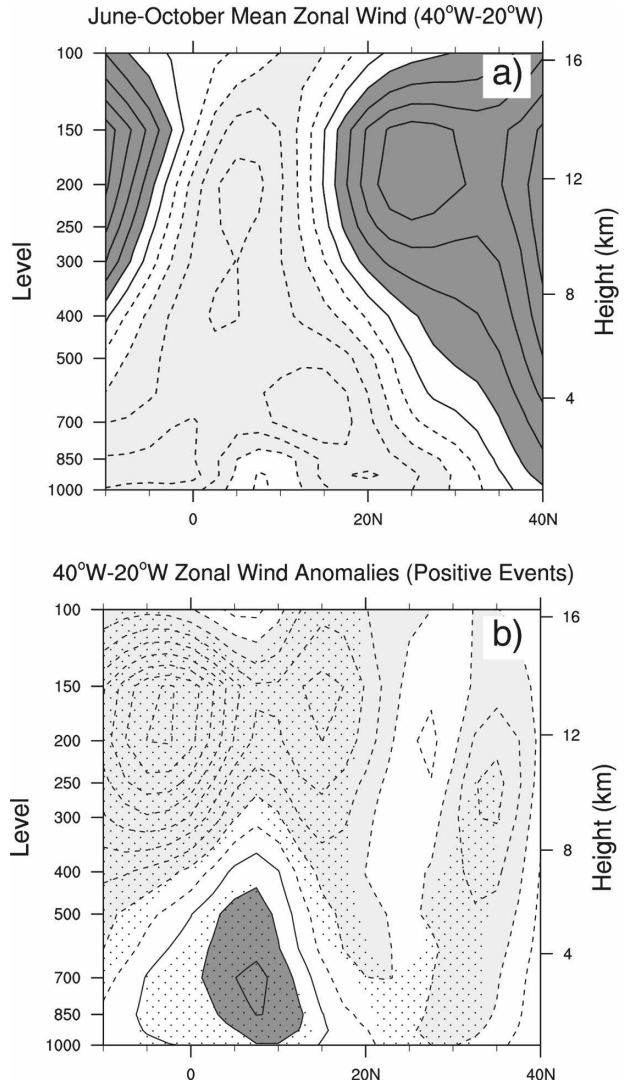


FIG. 6. (a) Mean vertical distribution of 40° – 20°W averaged zonal wind during June–October and (b) composite 40° – 20°W averaged zonal wind anomalies for positive 30–90-day precipitation events. The contour interval in (a) is 2 m s^{-1} , starting at 1 m s^{-1} . Values greater (less) than 3 m s^{-1} (-3 m s^{-1}) are dark (light) shaded. The contour interval in (b) is 0.5 m s^{-1} , starting at 0.25 m s^{-1} . Values greater (less) than 0.75 m s^{-1} (-0.75 m s^{-1}) are dark (light) shaded. Stippling in (b) indicates where zonal wind anomalies are significantly different from zero at the 95% confidence level.

variations may impact tropical cyclone activity in the east Atlantic is examined in more detail in section 5.

Figure 7 indicates that wind anomalies along 0° (10°W – 10°E averaged) are generally weaker than those in the Atlantic during 30–90-day precipitation events. This also remains true when examining a time-lagged analysis (not shown). While low-level wind anomalies are significant from the equator to 10°N , they are generally weak. Upper-tropospheric wind anomalies are

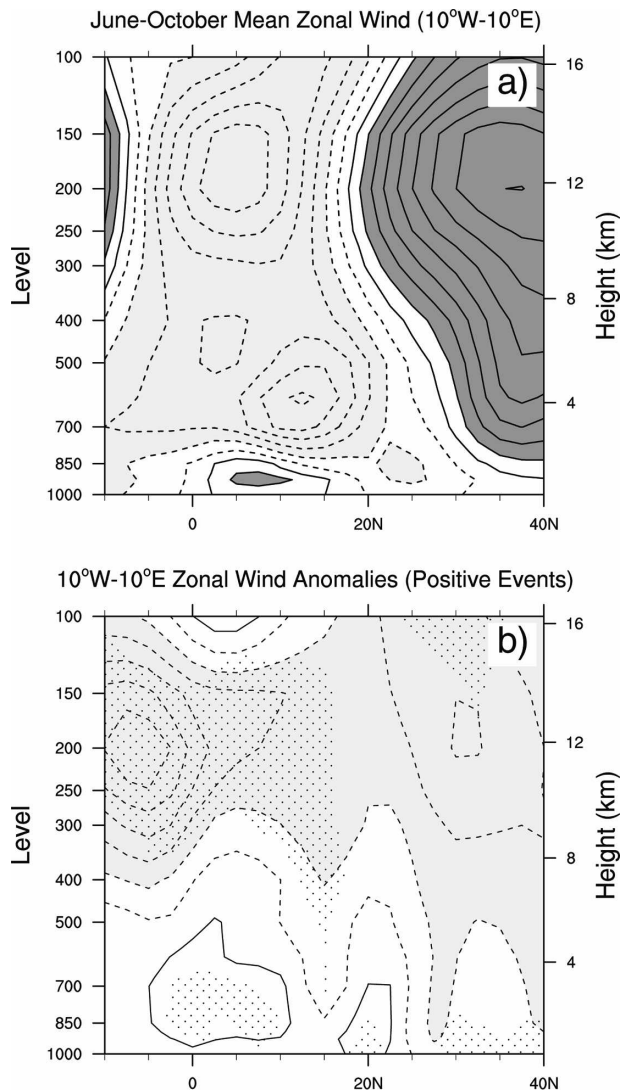


FIG. 7. Same as Fig. 6, but for 10°W–10°E averages.

generally stronger than those in the lower troposphere, with strong easterly anomalies occurring to the south of the tropical easterly jet centered near 175 hPa and 5°N. No significant modulation of the African easterly jet (AEJ, centered near 600 hPa and 12°N, e.g., Cook 1999) occurs during 30–90-day precipitation events, and changes in meridional shear of the zonal wind at the southern flank of the jet also appear to be weak. We used NCEP reanalysis to analyze the evolution of the IPV gradient on the 315 K theta surface over West Africa during 30–90-day precipitation events. Combined barotropic/baroclinic instability associated with reversal of the IPV gradient on the south flank of the AEJ is important to AEW energetics (e.g., Thorncroft and Hoskins 1994a,b). While results hinted that the strength of the IPV gradient reversal on the south flank of the

AEJ maximizes about 5–10 days after positive 30–90-day precipitation events, results were generally inconclusive and not significant. Further analysis of the PV dynamics of the west African monsoon region on intraseasonal time scales will be conducted in future work, including use of a higher-resolution dataset to better resolve tight IPV gradients associated with the AEJ.

We also tested the hypothesis that the conditions favorable for inertial instability are modulated on 30–90-day time scales. Tomas and Webster (1997) hypothesize that excursion of the zero absolute vorticity contour to the north of the equator fosters inertial instability, manifest as a divergent 925-hPa circulation accompanied by rising motion and enhanced precipitation to the north of the zero absolute vorticity line, and subsidence near the equator. Because the intraseasonal convective center in the Gulf of Guinea (Fig. 5) lies near the climatological zero absolute vorticity line (e.g., Tomas and Webster 1997), we wanted to test whether intraseasonal variations in 30–90-day convective activity might be supported by fluctuations in absolute vorticity and associated divergent circulations. Our analysis found little coherent intraseasonal variability in the zero absolute vorticity contour and related divergent circulations about their mean states, making inertial instability an unlikely mechanism for the strong 30–90-day precipitation variability that we see in the Gulf of Guinea and Atlantic ITCZ.

Composite surface EKE anomalies during positive and negative 30–90-day precipitation events are shown in Fig. 8. Because the strongest EKE anomalies occur at a lag of 5 days relative to the extrema of the 30–90-day precipitation time series, composite EKE anomalies are shown at a 5-day lag. Stippling indicates where EKE anomalies are significantly different from zero at the 95% confidence limit. Associated with southwesterly flow anomalies in the Atlantic ITCZ region during positive precipitation events, a significant enhancement of EKE occurs. Positive EKE anomalies are also found in West Africa centered near 0°E, although the amplitude of these anomalies is generally weak. EKE anomalies of the opposite sense occur during negative precipitation events. An analysis using QuikSCAT vector winds indicates significant EKE anomalies in similar oceanic locations to those shown in Fig. 8, though the QuikSCAT EKE anomalies tend to be stronger than those from NCEP reanalysis. We also note that surface EE anomalies show a significant modulation in similar areas to EKE, although EE is not shown here for brevity. This similarity in EE and EKE behavior can also be inferred from the spectra in Fig. 3 and is not particularly surprising given the dominant eddy structure shown in

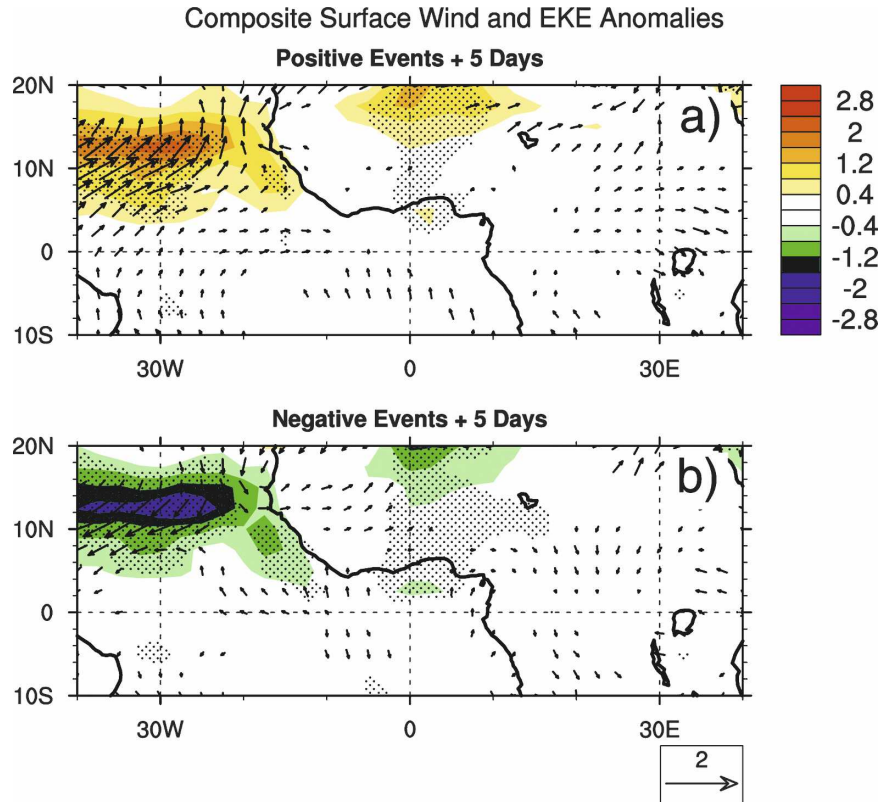


FIG. 8. Composite EKE and surface wind anomalies for (a) positive (+5 days) and (b) negative (+5 days) 30–90-day precipitation events. EKE anomaly units are $\text{m}^2 \text{s}^{-2}$. The reference vector in m s^{-1} is shown at the bottom right. Stippling indicates where EKE anomalies are significantly different from zero at the 95% confidence level. Only wind vectors significant at the 95% confidence level are shown.

Fig. 9. The location of strongest surface EKE anomalies during 30–90-day precipitation events is over the Atlantic to the west of Africa, whereas the analysis of Matthews (2004) showed that 700-hPa meridional velocity variance exhibits the strongest variations over Africa. This difference is not entirely surprising, given observations from the Global Atmospheric Research Program (GARP) Atlantic Tropical Experiment showing that surface signatures of AEWs are much stronger over ocean than over land (Reed et al. 1977), possibly because of decreased surface friction over the water.

Surface EKE variations are likely caused by variations in AEWs or associated tropical cyclones that may be spawned. To support this contention, we examine the dominant eddy structures during positive 30–90-day precipitation events through linear regression. Eddy vorticity and eddy wind components are regressed onto eddy vorticity at 12.5°N , 27.5°W during the periods of strongest EE and EKE represented in Fig. 8, including data within the 5-day period centered 5 days after the peak of the precipitation events. Regression coefficients

are then scaled by 1σ , where σ represents the standard deviation of the eddy vorticity at 12.5°N , 27.5°W during positive precipitation events. Figure 9 shows the dominant eddy structure. The eddies are characterized by structures with zonal wavelengths of

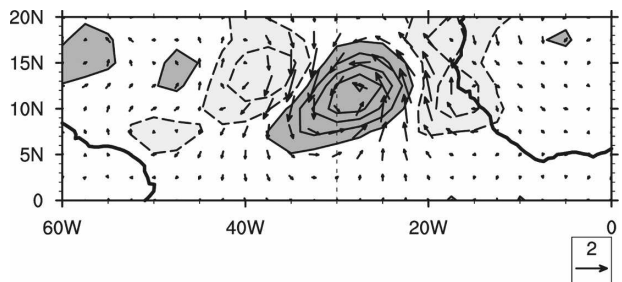


FIG. 9. Regression of eddy vorticity and eddy surface winds onto the eddy vorticity time series at 12.5°N , 27.5°W for positive 30–90-day precipitation events (+5 days). Contours are plotted every $1.8 \times 10^{-6} \text{ s}^{-1}$, starting at $0.9 \times 10^{-6} \text{ s}^{-1}$. Values greater (less) than $0.9 \times 10^{-6} \text{ s}^{-1}$ ($-0.9 \times 10^{-6} \text{ s}^{-1}$) are dark (light) shaded. The reference wind vector is shown at the bottom right.

about 2500 km. Individual vorticity centers have a southwest–northeast tilt with latitude, resembling the AEWs that have been extensively documented in the literature (e.g., Riehl 1954; Burpee 1972, 1974; Reed et al. 1977; Albignat and Reed 1980). In addition, the eddies shown in Fig. 9 occur in the band 10° – 15° N, where the track density of easterly waves in the Atlantic is also primarily concentrated (Thorncroft and Hodges 2001).

b. Complex EOF analysis

The evolution of precipitation anomalies associated with 30–90-day precipitation events can be compactly described using Hilbert transform CEOF analysis (e.g., Barnett 1983; Horel 1984). While similar to standard EOF analysis, CEOF analysis is conducted using a covariance matrix constructed from the complex analytic function at each grid point in the domain of interest. The complex analytic function consists of the time series at each grid point in the domain of interest plus its quadrature function times i . A propagating signal can thus be represented by a single CEOF, instead of two EOFs. Maloney et al. (2008) describe the use of CEOF analysis in significant detail for the case of covariability of east Pacific intraseasonal SST and precipitation during boreal summer.

We first bandpass-filter the TRMM precipitation field to 30–90 days and then compute the quadrature function (temporal Hilbert transform) over the entire time series (1998–2006) to construct the analytic signal. The covariance matrix for use in the CEOF analysis is then constructed using June–October precipitation data over the domain 10° S– 20° N, 40° W– 40° E. We choose a larger domain than used for the regional precipitation time series described above to avoid predetermining the results of the CEOF analysis and to independently verify the validity of the averaging box used to calculate the regional time series. The structure and propagation characteristics of the leading CEOFs are not sensitive to reasonable variations in the size of the spatial domain. The CEOF analysis results in amplitude time series and spatial CEOFs that are complex, allowing spatial and temporal phase and amplitude information to be derived in a straightforward manner.

Figure 10 describes the leading CEOF, which explains 11.8% of the variance. This leading CEOF is distinguishable from the second CEOF (8.2%) using the criterion of North et al. (1982) and assuming that every 50 days is an independent sample for about 27 degrees of freedom during June–October of 1998–2005. We have further confidence that the leading CEOF explains a physical mode of variability because the spatial

structure and temporal evolution described by this CEOF resembles that derived by composite analysis using the regional 30–90-day precipitation time series described above (although this evolution is not explicitly shown). We note that a similar CEOF analysis of boreal summer 30–90-day precipitation for a similar size domain in the east Pacific warm pool produces a leading CEOF that explains 26% of the variance (Maloney et al. 2008), and so the 30–90-day mode of variability we show here is less dominant than that derived for other tropical regions.

Spatial amplitudes associated with CEOF1 are generally strong in regions of high mean precipitation shown in Fig. 1, with the highest amplitude in the Gulf of Guinea and at the western African coast near 6° N, 15° W (Fig. 10a). The variance explained by CEOF1 exceeds 30% locally, with the largest explained variance occurring in the Gulf of Guinea, near the West African coast along 6° N, and to the north of 10° N on the north side of the Atlantic ITCZ (Fig. 10b).

Temporal phases (not shown here) associated with the leading CEOF vary between -180° and 180° and generally increase monotonically with time, completing one cycle approximately every 40–50 days. Combined with the temporal phase, the spatial phases in Fig. 10c describe the temporal evolution of 30–90-day precipitation anomalies in the West African monsoon region during boreal summer and also resemble the composite evolution of precipitation anomalies associated with the regional 30–90-day precipitation index (not shown). Spatial phase in Fig. 10c is only shown where the local variance explained exceeds 5%. Precipitation anomalies appear to be initiated in a couple of isolated regions: in a narrow band extending southwestward from 14° N, 10° W and over central Africa near 4° N, 20° E. By a bit less than 1/4 cycle later (with some modest phase variations), same-signed precipitation anomalies have enveloped much of the region bounded by 0° – 14° N, 35° W– 20° E. To first order, the evolution of 30–90-day precipitation anomalies primarily resembles a stationary pulsing of precipitation at the locations of high mean precipitation. This behavior is a motivation for using the 0° – 14° N, 35° W– 20° E averaging box to define our regional 30–90-day regional precipitation time series. Interestingly, however, Fig. 10c does suggest the possibility that the Gulf of Guinea and the Atlantic ITCZ contain distinct 30–90-day convective centers. Further, the strong dynamical signal associated with the Atlantic convective center (e.g., Figure 5) and the lack of a strong dynamical signal associated with the Gulf of Guinea center suggest the possibility of distinct convective regulation mechanisms. However, given the simi-

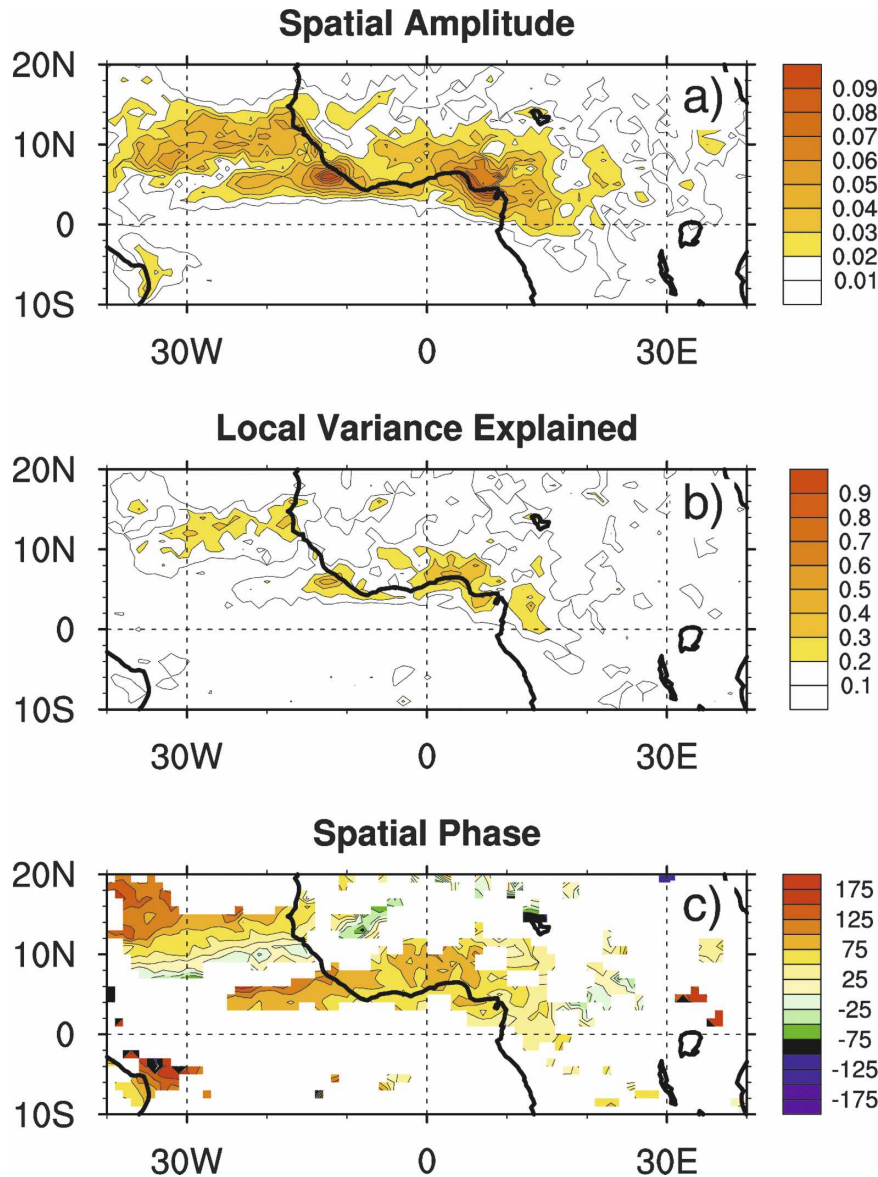


FIG. 10. (a) Spatial amplitude, (b) fraction of local variance explained, and (c) spatial phase corresponding to the first CEOF of June–October 30–90-day precipitation. The CEOF analysis was conducted on the domain shown. The spatial amplitude was normalized in the calculation of the CEOFs. Increasing spatial phase indicated the direction of propagation for increasing temporal phase.

larity in phase between the Gulf of Guinea and the Atlantic ITCZ during 30–90-day precipitation events (as determined both through CEOF analysis and composite analysis), we do not separately consider these two regions here. Examination of whether different processes regulate intraseasonal convective variability in these two regions will be left to future work.

The correspondence between CEOF1 and the regional precipitation time series can be further supported by examining how their respective amplitudes

vary with time (Fig. 11). The amplitude of the 30–90-day precipitation time series (generated by squaring the time series, applying a 41-day running mean smoother, and taking the square root) generally follows that of the leading CEOF. A synthesized oscillating time series that includes both amplitude and phase information for CEOF1 can be generated by multiplying the temporal amplitude by the cosine (or sine) of temporal phase. When this synthesized CEOF time series is correlated with the 30–90-day precipitation time series, it is corre-

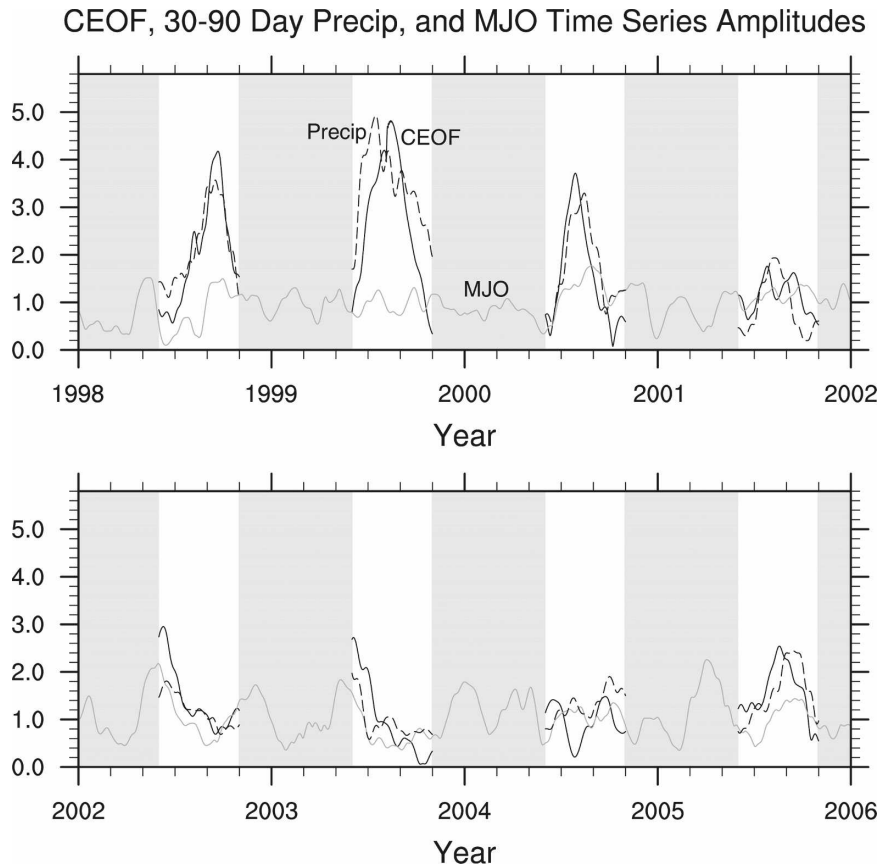


FIG. 11. Amplitudes for precipitation CEOF1 (black solid), the 30–90-day precipitation time series (black dashed), and the equatorial MJO time series (gray solid). June–October periods are highlighted in white, and gray shading covers the rest of the year; 2006 is omitted from the figure for display purposes.

lated at +0.8. Interestingly, Fig. 11 indicates that the amplitude of 30–90-day precipitation variability in the West African monsoon region exhibits large interannual fluctuations. Strong local intraseasonal oscillations occurred during the summers 1998–2000, whereas relatively weak activity existed during 2002–04. The amplitude of the equatorial MJO time series described above is also shown on the plot. The fluctuations in strength of 30–90-day intraseasonal variability in West Africa show no consistent relationship to the amplitude of the MJO index. Even if the MJO is a significant influence on intraseasonal variability in the African monsoon region as suggested above, regional processes are clearly playing a role to modify its influence or to generate 30–90-day intraseasonal variability that is independent of the MJO.

5. Variations in tropical cyclones

As suggested by Figs. 8, 9, the significant 30–90-day variations in EKE and AEWs between 10° and 20° N to

the east of 60° W may also indicate a modulation of tropical cyclone activity, because the main development region for tropical cyclones is located here (e.g., Goldenberg and Shapiro 1996). Landsea et al. (1998) found that 17 of the 19 Atlantic tropical cyclones during the active year of 1995 formed from AEWs. While Mo (2000) noted a statistically significant modulation of TCs by the MJO to the east of 60° W (see her Fig. 5b), the most robust modulation of tropical cyclone activity occurred over the western part of the Atlantic, also consistent with the results of Maloney and Hartmann (2000b). Here, we examine the modulation of east Atlantic tropical cyclones (east of 60° W) during strong 30–90-day precipitation events, with the understanding that not all of the tropical cyclone variability associated with the regional 30–90-day precipitation time series is caused by the global MJO (per the analysis of Fig. 4).

Figures 12a,b show differences in cyclone activity during periods of enhanced and suppressed tropical cyclone activity relative to maxima in the regional pre-

Composite Tropical Cyclone Locations

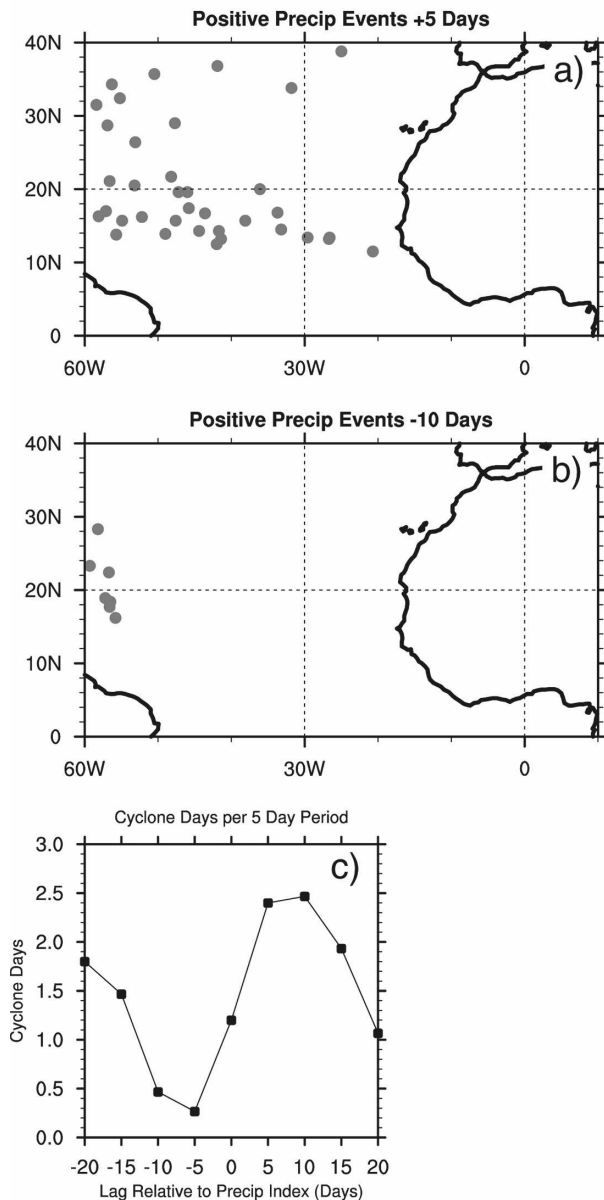


FIG. 12. Accumulated daily TC reports within 5-day periods centered on (a) day +5 and (b) day -10 relative to positive 30–90-day precipitation events defined by the regional time series. Cyclone reports are accumulated across all 15 positive precipitation events. Considering each cyclone independently, the markers correspond to the first recorded cyclone location on a given day. (c) The composite number of tropical cyclone days per 5-day period as a function of lag relative to positive 30–90-day precipitation events, which includes Atlantic cyclones to the east of 60°W.

precipitation time series. A marker is plotted for any daily report of a tropical cyclone (>35 kt) within the 5-day periods centered at day +5 (Fig. 12a) and day -10 (Fig. 12b) relative to the time series maxima. The markers

correspond to the first recorded position on a given day. The choices of which time lags to display are based on Fig. 12c, described in the next paragraph. An enhancement of tropical cyclone activity occurs to the east of 60°W, which peaks about 5 days after regional precipitation time series maxima. Likewise, a suppression of tropical cyclone activity occurs about 10 days before maxima in the precipitation time series. The largest differences in cyclone activity between the time lags displayed occur between 10° and 20°N in the MDR (Goldenberg and Shapiro 1996), where the differences in cyclone genesis statistics are just as notable (not shown). Note that the time of peak precipitation in the MDR does not necessarily coincide with when the regional precipitation time series maximizes, as is suggested in Fig. 10. As described in Fig. 12c, cyclone counts at day +5 and day +10 in the domain shown are very similar. We choose to display a day +5 map rather than a day +10 map because many of the cyclones at day +10 appear to capture cyclones that originated in the MDR at previous times and then moved northwest. Similarly, we display a day -10 map rather than a day -5 map because cyclone activity is a minimum in the MDR at day -10 relative to day -5.

To assess statistical significance of the cyclone modulation on 30–90-day time scales, we plot the composite number of east Atlantic tropical cyclone days per a 5-day period as a function of time lag relative to maxima in the regional precipitation time series (Fig. 12c). Related to the definition of Gray (1998), we define a tropical cyclone day as any day when a tropical system exists to the east of 60°W that achieves at least tropical storm status (winds greater than 35 kt). A given day can contribute more than one cyclone day if more than one tropical cyclone exists on that day. Given the 15 positive precipitation events that go into the composite and using a *t* test for the difference between means that takes into account information about the sample means and variances about the means, the differences in east Atlantic cyclone days between periods of enhanced tropical cyclone activity (e.g., day +5 or day +10) and suppressed tropical cyclone activity (e.g., day -5 or day -10) are statistically significant at the 95% confidence level. We note that a similar but opposite-signed modulation of tropical cyclones as shown in Fig. 12c occurs when events are defined based on regional precipitation time series minima, with the exception that tropical cyclone activity minimizes about 15 days after minima in the precipitation time series. Thus, it appears that tropical cyclone activity in the east Atlantic cyclone development region is significantly modulated by the 30–90-day oscillation over this region, which is related in part to the MJO. This relation-

ship mirrors findings at interannual and multidecadal time scales, where previous studies have shown a significant relationship between West African monsoon rainfall and Atlantic hurricane activity (e.g., Landsea and Gray 1992; Goldenberg and Shapiro 1996; Bell and Chelliah 2006).

Figure 13 shows a similar analysis to Fig. 12, except that composites are generated from significant positive events in the equatorial MJO index. Using the results of Fig. 4, the MJO index is shifted back in time by 10 days for consistency with the regional precipitation time series. Strong June–October extrema of the MJO index with magnitude greater than 1σ are selected, for a total of 15 positive MJO events during 1998–2006. Here, 8 of the 15 positive events defined by the regional precipitation time series occur within 5 days to either side of positive MJO events.

Figure 13 shows that the amplitude of the tropical cyclone modulation by the MJO is similar to that when using the regional precipitation time series to define events. Tropical cyclone activity peaks about 5 days after the MJO index, when it shows greatest concentration in the MDR. Tropical cyclone activity is suppressed about 10 days before maxima in the MJO index. Although this analysis does not directly indicate how much of the tropical cyclone variability associated with the regional time series is attributable to the MJO, it does indicate that both global and local measures of intraseasonal variability are associated with similar amplitude modulations of Atlantic tropical cyclone activity. This finding is important because the slowly evolving tropical wind and precipitation anomalies associated with the MJO are potentially predictable 2–3 weeks in advance (e.g., Waliser et al. 1999).

Although we have not conducted a comprehensive analysis of how intraseasonal precipitation variability of the West African monsoon modulates tropical cyclone activity to the east of 60°W , one hypothesis is that vertical shear variations are important. A similar hypothesis was developed by Mo (2000). For this analysis, we define vertical shear as the magnitude of the difference between the (unfiltered) 850-hPa and 200-hPa wind vectors. Figure 14 shows that the difference in composite vertical shear between peak negative and positive phases of the regional precipitation time series exceeds 6 m s^{-1} in the region of most concentrated positive precipitation event cyclone activity shown in Fig. 12. Total shear in this region of concentrated cyclone activity is about 10 m s^{-1} during positive precipitation events and exceeds 16 m s^{-1} during negative precipitation events. The suppression of shear in the MDR at day +5 relative to the maximum in the precipitation time series is of similar magnitude to that at the maximum itself.

Composite Tropical Cyclone Locations

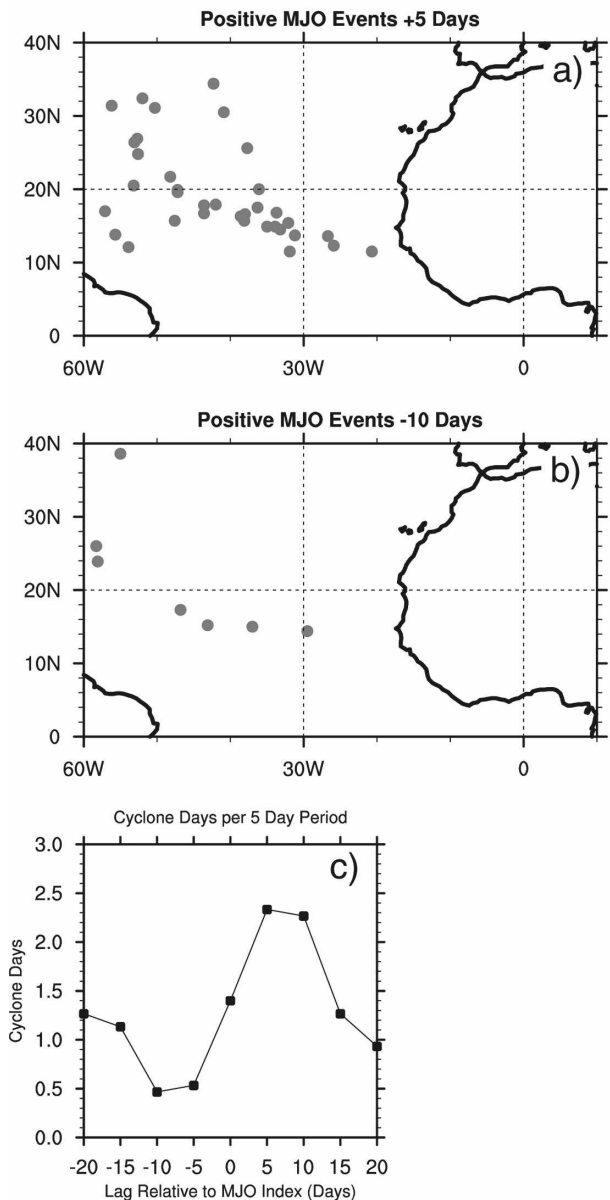


FIG. 13. Accumulated daily TC reports within 5-day periods centered on (a) day +5 and (b) day -10 relative to positive MJO events. Cyclone reports are accumulated across all 15 MJO events. Considering each cyclone independently, the markers correspond to the first recorded cyclone location on a given day. (c) The composite number of tropical cyclone days per 5-day period as a function of lag relative to positive MJO events, which includes Atlantic cyclones to the east of 60°W .

These shear variations are generally consistent with what would be expected from adding the composite first baroclinic mode zonal wind anomalies of Fig. 6 (and corresponding negative composite) to the mean flow. Observational findings and numerical results sug-

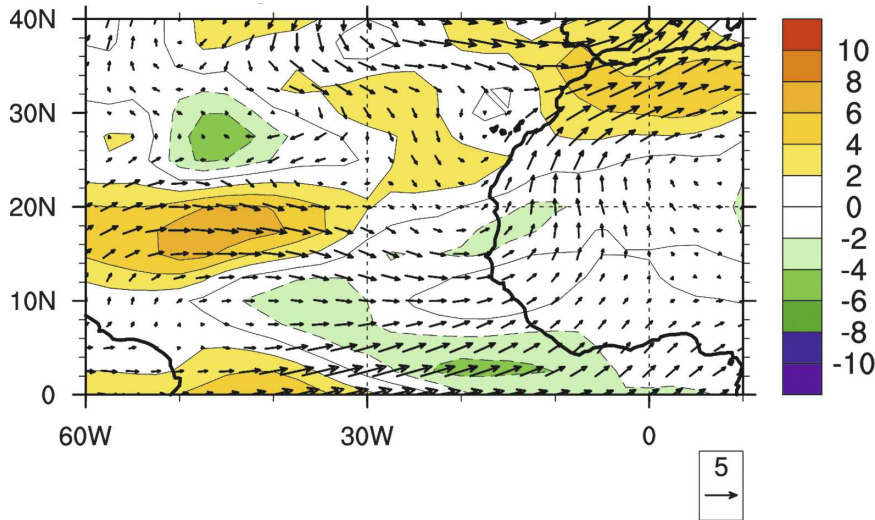


FIG. 14. Difference in composite vertical shear (m s^{-1}) and 200-hPa wind between negative and positive precipitation events as defined by the regional precipitation time series. The reference wind vector in m s^{-1} is shown at the bottom right.

gest that vertical shears of greater than 10 m s^{-1} have an immediate deleterious impact on developing tropical systems (e.g., Zehr 1992; Frank and Ritchie 2001). Vertical shear was also shown to be an important link between the interannual modulation of West African rainfall and Atlantic tropical cyclone activity (Goldenberg and Shapiro 1996), and it also appears to be important to TC modulation in the Atlantic MDR on multi-decadal time scales (e.g., Vimont and Kossin 2007).

We used partial regression analysis (e.g., Goldenberg and Shapiro 1996) to determine what fraction of the MDR vertical shear variations of Fig. 14 could be explained by the equatorial MJO index. When a partial regression analysis is conducted between the regional precipitation time series and 30–90-day shear anomalies in which the shear variance explained by the equatorial MJO index is removed, the amplitude of the regression coefficient in the MDR is reduced by 50% as compared to the total regression coefficient. Thus, it appears that the MJO accounts for a sizeable fraction of the vertical shear variations in the MDR during regional 30–90-day precipitation events.

6. Conclusions and discussion

Intraseasonal variability of the West African monsoon is examined during June–October of 1998–2006 using TRMM precipitation and NCEP reanalysis winds. A spectral analysis indicates that intraseasonal precipitation variability is dominated by two distinct time scales with significant spectral peaks centered near periods of 15 days and 50 days. These time scales

are consistent with those found in other studies. Eddy kinetic energy and eddy enstrophy in the Atlantic tropical cyclone genesis region also show significant spectral peaks at these same frequencies. The research presented here concentrates on variability associated with the 50-day peak, approximately bracketed by 30–90-day time scales.

Precipitation variability on 30–90-day time scales in West Africa and the eastern Atlantic is significantly correlated with a global time series of the MJO, supporting the hypothesis of Matthews (2004) that the MJO significantly modulates convection in the West African monsoon region during boreal summer. The MJO explains about 30% of the 30–90-day precipitation variance in the west African monsoon region.

Composite analysis and complex empirical orthogonal function analysis show that 30–90-day precipitation anomalies are generally zonally elongated, grow and decay in place, and have maximum amplitude in the Gulf of Guinea and the Atlantic ITCZ. Enhanced precipitation events are accompanied by a significant weakening of North Atlantic trade winds, and suppressed precipitation events are accompanied by significant enhancement of the trades. Zonal wind anomalies in the upper troposphere are 180° out of phase with those near the surface. The amplitude of 30–90-day precipitation variability changes greatly from summer to summer, with some years exhibiting strong variability and other years having very weak variability.

Weakening of Atlantic trades during positive 30–90-day precipitation events is accompanied by enhanced surface eddy kinetic energy in the main development

region for tropical cyclones in the Atlantic between 10° and 20° N, with the strongest eddy enhancement occurring 5 days after the peak of the precipitation event. The dominant eddies associated with enhanced precipitation events resemble African easterly waves. A comparable strong suppression of EKE occurs after the peak of 30–90-day suppressed precipitation events.

A significant modulation of TC activity occurs in association with the 30–90-day oscillation. The number of tropical cyclones that occur in the Atlantic MDR to the east of 60° W is suppressed about 5–10 days before the maxima in a regional intraseasonal precipitation time series and is enhanced about 5–10 days after the time series maxima. A similar but opposite-signed modulation occurs when negative precipitation events are used to composite TC activity. The number of tropical cyclones reported is about 5 times greater in association with enhanced TC phases than suppressed TC phases, a result statistically significant at the 95% confidence level. When compositing TC activity based on an equatorial MJO index, similar amplitude and phase modulation are obtained. These findings are consistent with those of Mo (2000). Variations in vertical shear in the MDR may help to explain this modulation of tropical cyclones. The MJO is responsible for about half of the amplitude of vertical shear variations in the Atlantic MDR during 30–90-day precipitation events.

Future work will examine the physical mechanisms responsible for the significant 30–90-day modulation of precipitation that occurs over the African monsoon region during boreal summer. Here, we preliminarily assessed several possible mechanisms that may contribute to intraseasonal precipitation variability in the West African monsoon region, some of which were proposed by Matthews (2004).

First, we analyzed whether organized variations in the boundary layer monsoon flow and associated moisture convergence $[-\nabla \cdot (q\mathbf{v})]$ could generate large-scale forcing for precipitation anomalies. A comparison of Figs. 1 and 5 indicates that the boundary layer southwesterly flow is only weakly enhanced in most of the African monsoon region during periods of enhanced precipitation, and in regions of significant precipitation anomalies boundary layer flow anomalies are often not significant. Further, an analysis of boundary layer moisture convergence (not shown) indicates that moisture convergence is indeed enhanced in patchy regions near the strongest precipitation anomalies, but these convergence anomalies indicate no large-scale coherence that would suggest organized dynamical forcing. The moisture convergence anomalies may more likely be a by-product of convective heating rather than a cause (e.g.,

Neelin and Held 1987). An analysis at 925 hPa produces similar results.

Second, also relevant to boundary flow variations, we tested the hypothesis that the conditions favorable for inertial instability are modulated on 30–90-day time scales, which in turn could modulate intraseasonal precipitation (e.g., Tomas and Webster 1997). Neither the boundary layer divergence nor the position of the zero absolute vorticity line showed variations that suggested inertial instability is important to intraseasonal variability in this region (see also section 4a).

The 700-hPa flow does exhibit stronger westerly enhancement than at the surface during periods of enhanced precipitation, consistent with Matthews (2004). Stronger easterly, offshore flows occur during periods of suppressed precipitation. A third hypothesis is the interesting possibility that such enhanced offshore flow may advect dry, dusty air associated with the Saharan air layer over the ocean, which may suppress precipitation there. Recent studies have documented links between Sahel rainfall, the Saharan air layer, and Atlantic TC activity (e.g., Dunion and Velden 2004; Evan et al. 2006; Wu 2007). Although 700-hPa wind and specific humidity fields from NCEP reanalysis do not indicate widespread enhanced dry advection during suppressed precipitation events, we hope to explore this hypothesis further in future work.

As noted in section 4a, a fourth hypothesis we examined is whether intraseasonal flow variations near the 700-hPa level could generate significant variations in the IPV gradient. Such variations could impact easterly wave growth and development, and easterly waves are associated with significant convective variability. While results hinted that the strength of the 315-K IPV gradient reversal on the south flank of the AEJ maximizes about 5–10 days after positive 30–90-day precipitation events, these results were generally inconclusive and not significant. However, synoptic-scale wave activity is enhanced in association with positive 30–90-day precipitation events (e.g., Figs. 8, 9). Kiladis et al. (2006) and Hall et al. (2006) showed that easterly waves in West Africa and the Atlantic generate precipitation anomalies that are in phase with the adiabatic dynamical forcing provided by the waves. Presumably, periods of enhanced easterly wave activity on intraseasonal time scales could have upscale influences on precipitation in the 30–90-day band.

Last, we examined the influence of upper-level dynamical features for forcing intraseasonal convection. The most coherent fluctuations associated with 30–90-day precipitation events in the West African monsoon region appear to occur at upper levels. Matthews (2004) hypothesized that MJO convective heating over the

west Pacific warm pool forces atmospheric Kelvin waves that propagate into the Atlantic, cooling the upper and midtroposphere and thus fostering convective instability. Figure 15 shows composite equatorial 30–90-day bandpass-filtered 200-hPa zonal wind, 700-hPa zonal wind, and 300-hPa temperature anomalies as a function of lag in days relative to maxima in the regional precipitation time series. Also indicated are regions where composite precipitation anomalies are significantly different from zero at the 95% confidence level (stippling). Eastward propagation is more or less continuous in 200-hPa zonal wind and 300-hPa temperature from the west Pacific warm pool into the West African monsoon region, consistent with the hypothesis of Matthews (2004) that intraseasonal heating in the west Pacific warm pool forces Kelvin waves that influence the West African monsoon. As in Matthews (2004), cold upper-tropospheric temperature anomalies generated by the upwelling Kelvin waves appear to support convective enhancement during positive 30–90-day precipitation events. Propagation in the lower troposphere is less continuous and appears to be severely disrupted by the Andes near 75°W. Although Atlantic and West African precipitation anomalies are most likely initiated by upper-level processes, winds in the lower troposphere appear to respond locally. Such lower-tropospheric wind anomalies may provide feedbacks onto local precipitation.

It is interesting that the eastward propagation speeds of 300-hPa temperature and 200-hPa zonal wind anomalies appear to be different (Fig. 15). From 150°W to 0°, the average propagation speed of the temperature anomaly is 32 m s^{-1} , consistent with rapid eastward propagation of temperature signals away from suppressed intraseasonal convection in the west Pacific warm pool (e.g., Matthews 2000, 2004; Heckley and Gill 1984). The 200-hPa zonal wind signature propagates eastward at about 16 m s^{-1} . While the negative temperature and wind anomalies are initiated in the west Pacific warm pool at different times, they reach the African monsoon region nearly in unison. The different propagation speeds of intraseasonal zonal wind and temperature anomalies are not surprising given the results of Bantzer and Wallace (1996, 3035–3037), who showed that eastward-propagating wind anomalies directly related to the MJO move more slowly than the radiating temperature response to west Pacific MJO heating anomalies. MJO wind anomalies may be further slowed in the east Pacific during boreal summer because of strong interactions with intraseasonal convection in the east Pacific warm pool (e.g., Maloney and Hartmann 2000a).

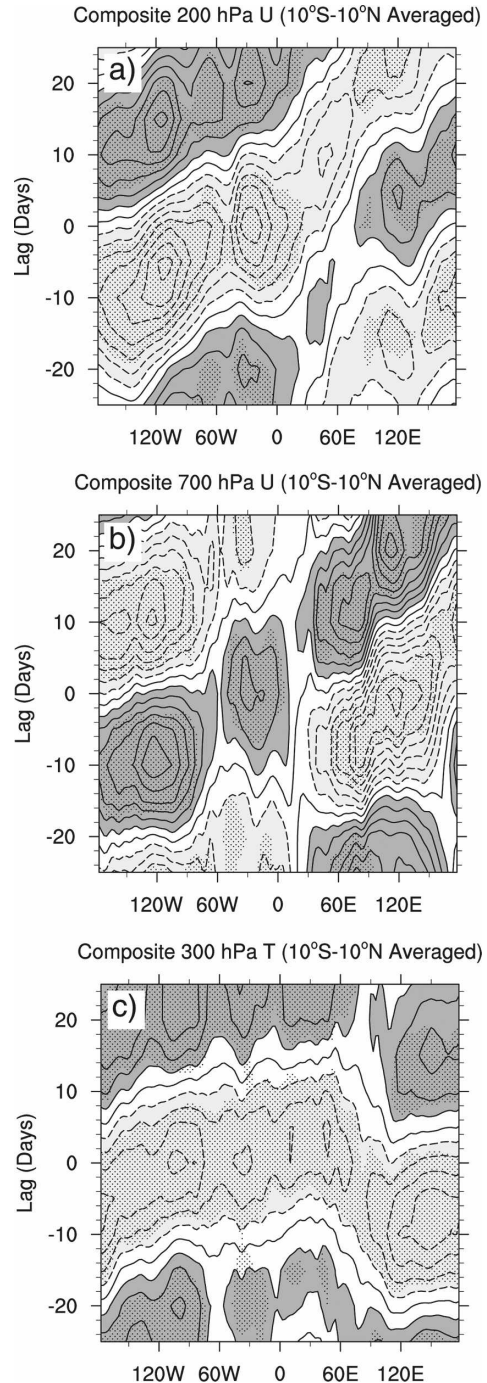


FIG. 15. Composite equatorial (10°N – 10°S averaged) 30–90-day bandpass-filtered (a) 200-hPa zonal wind, (b) 700-hPa zonal wind, and (c) 300-hPa temperature anomalies as a function of lag in days relative to positive precipitation events as defined by the regional precipitation time series. The contour interval in (a) is 0.6 m s^{-1} , with values greater (less) than 0.6 (-0.6) being dark (light) shaded. The contour interval in (b) is 0.2 m s^{-1} , with values greater (less) than 0.2 (-0.2) being dark (light) shaded. The contour interval in (c) is 0.1°C , with values greater (less) than 0.1 (-0.1) being dark (light) shaded. Stippling indicates where anomalies are significantly different from zero at the 95% confidence level.

Regardless of the mechanisms, a significant modulation of precipitation and tropical cyclones occurs on intraseasonal time scales in the eastern Atlantic. Because a significant portion of this variability is associated with global modes of variability such as the MJO that may be predictable 2–3 weeks in advance (e.g., Waliser et al. 1999; Jones et al. 2004), the results of this study and others (e.g., Maloney and Hartmann 2000b; Mo 2000) may have important consequences for prediction of tropical cyclone activity in the Atlantic basin.

Acknowledgments. Three anonymous reviewers provided insightful comments on the manuscript. This work was supported by the Climate and Large-Scale Dynamics Program of the National Science Foundation (NSF) under Grants ATM-0540901 and ATM-0632341, and under Award# NA05OAR4310006 from the National Oceanic and Atmospheric Administration (NOAA), U.S. Department of Commerce. The statements, findings, conclusions, and recommendations do not necessarily reflect the views of NSF, NOAA, or the Department of Commerce. The authors wish to thank the TRMM Science Data and Information System and the Distributed Active Archive Center for providing the TRMM precipitation fields. NCEP/NCAR reanalysis data were provided by NOAA/OAR/ESRL PSD, Boulder, Colorado.

REFERENCES

- Albignat, J. P., and R. J. Reed, 1980: The origin of African wave disturbances during phase III of GATE. *Mon. Wea. Rev.*, **108**, 1827–1839.
- Annamalai, H., and J. M. Slingo, 2001: Active/break cycles: Diagnosis of the intraseasonal variability of the Asian summer monsoon. *Climate Dyn.*, **18**, 85–102.
- Bantzer, C. H., and J. M. Wallace, 1996: Intraseasonal variability in tropical mean temperature and precipitation and their relation to the tropical 40–50-day oscillation. *J. Atmos. Sci.*, **53**, 3032–3045.
- Barnett, T. P., 1983: Interaction of the monsoon and Pacific trade wind system at interannual time scales. Part I: The equatorial zone. *Mon. Wea. Rev.*, **111**, 756–773.
- Bell, G. D., and M. Chelliah, 2006: Leading tropical modes associated with interannual and multidecadal fluctuations in North Atlantic hurricane activity. *J. Climate*, **19**, 590–612.
- Burpee, R. W., 1972: The origin and structure of easterly waves in the lower troposphere of North Africa. *J. Atmos. Sci.*, **29**, 77–90.
- , 1974: Characteristics of North African easterly waves during the summers of 1968 and 1969. *J. Atmos. Sci.*, **31**, 1556–1570.
- Camargo, S. J., K. A. Emanuel, and A. H. Sobel, 2007: Use of a genesis potential index to diagnose ENSO effects on tropical cyclone genesis. *J. Climate*, **20**, 4819–4834.
- Chelton, D. B., and M. H. Freilich, 2005: Scatterometer-based assessment of 10-m wind analyses from the operational ECMWF and NCEP numerical weather prediction models. *Mon. Wea. Rev.*, **133**, 409–429.
- Cook, K. H., 1999: Generation of the African easterly jet and its role in determining West African precipitation. *J. Climate*, **12**, 1165–1184.
- DeMaria, M., 1996: The effect of vertical shear on tropical cyclone intensity change. *J. Atmos. Sci.*, **53**, 2076–2087.
- Dunion, J. P., and C. S. Velden, 2004: The impact of the Saharan air layer on Atlantic tropical cyclone activity. *Bull. Amer. Meteor. Soc.*, **85**, 353–365.
- Evan, A. T., J. Dunion, J. A. Foley, A. K. Heidinger, and C. S. Velden, 2006: New evidence for a relationship between Atlantic tropical cyclone activity and African dust outbreaks. *Geophys. Res. Lett.*, **33**, L19813, doi:10.1029/2006GL026408.
- Foltz, G. R., and M. J. McPhaden, 2004: The 30–70 day oscillations in the tropical Atlantic. *Geophys. Res. Lett.*, **31**, L15205, doi:10.1029/2004GL020023.
- , and —, 2005: Mixed layer heat balance on intraseasonal time scales in the northwestern tropical Atlantic Ocean. *J. Climate*, **18**, 4168–4184.
- Frank, W. M., and E. A. Ritchie, 2001: Effects of vertical wind shear on the intensity and structure of numerically simulated hurricanes. *Mon. Wea. Rev.*, **129**, 2249–2269.
- Gilman, D., P. Fuglister, and J. M. Mitchell, 1963: On the power spectrum of red noise. *J. Atmos. Sci.*, **20**, 182–184.
- Goldenberg, S. B., and L. J. Shapiro, 1996: Physical mechanisms for the association of El Niño and West African rainfall with Atlantic major hurricane activity. *J. Climate*, **9**, 1169–1187.
- Gray, W. M., 1998: The formation of tropical cyclones. *Meteor. Atmos. Phys.*, **67**, 37–69.
- Grodsky, S. A., and J. A. Carton, 2001: Coupled land/atmosphere interactions in the West African monsoon. *Geophys. Res. Lett.*, **28**, 1503–1506.
- , —, and S. Nigam, 2003: Near surface westerly jet in the Atlantic ITCZ. *Geophys. Res. Lett.*, **30**, 2009, doi:10.1029/2003GL017867.
- Gu, G., and R. F. Adler, 2004: Seasonal evolution and variability associated with the West African monsoon system. *J. Climate*, **17**, 3364–3377.
- Hall, N. M. J., G. N. Kiladis, and C. D. Thorncroft, 2006: Three-dimensional structure and dynamics of African easterly waves. Part II: Dynamical modes. *J. Atmos. Sci.*, **63**, 2231–2245.
- Heckley, W. A., and A. E. Gill, 1984: Some simple analytical solutions to the problems of forced equatorial long waves. *Quart. J. Roy. Meteor. Soc.*, **110**, 203–217.
- Horel, J. D., 1984: Complex principal component analysis: Theory and examples. *J. Climate Appl. Meteor.*, **23**, 1660–1673.
- Huffman, G. H., R. F. Adler, M. M. Morrissey, D. T. Bolvin, S. Curtis, R. Joyce, B. McGavock, and J. Susskind, 2001: Global precipitation at one-degree daily resolution from multisatellite observations. *J. Hydrometeorol.*, **2**, 36–50.
- Janicot, S., and B. Sultan, 2001: Intraseasonal modulation of convection in the West African monsoon. *Geophys. Res. Lett.*, **28**, 523–526.
- Jarvinen, B. R., C. J. Neumann, and M. A. S. Davis, 1984: A tropical cyclone data tape for the North Atlantic Basin, 1886–1983: Contents, limitations, and uses. NOAA Tech. Memo. NWS NHC 22, 21 pp.
- Jenkins, G. M., and D. G. Watts, 1968: *Spectral Analysis and Its Applications*. Holden-Day, 525 pp.
- Jones, C., M. V. Carvalho, R. W. Higgins, D. E. Waliser, and J.-K. E. Schemm, 2004: A statistical forecast model of tropi-

- cal intraseasonal convective anomalies. *J. Climate*, **17**, 2078–2095.
- Kalnay, E., and Coauthors, 1996: The NCEP/NCAR 40-Year Reanalysis Project. *Bull. Amer. Meteor. Soc.*, **77**, 437–471.
- Kiladis, G. N., C. D. Thorncroft, and N. M. J. Hall, 2006: Three-dimensional structure and dynamics of African easterly waves. Part I: Observations. *J. Atmos. Sci.*, **63**, 2212–2230.
- Knutson, T. R., and K. M. Weickmann, 1987: 30–60 day atmospheric circulations: Composite lifecycles of convection and circulation anomalies. *Mon. Wea. Rev.*, **115**, 1407–1436.
- , —, and J. E. Kutzbach, 1986: Global-scale intraseasonal oscillations of outgoing longwave radiation and 250-mb zonal wind during Northern Hemisphere summer. *Mon. Wea. Rev.*, **114**, 605–623.
- Landsea, C. W., and W. M. Gray, 1992: The strong association between western Sahel monsoon rainfall and intense Atlantic hurricanes. *J. Climate*, **5**, 435–453.
- , G. D. Bell, W. M. Gray, and S. B. Goldenberg, 1998: The extremely active 1995 Atlantic hurricane season: Environmental conditions and verification of seasonal forecasts. *Mon. Wea. Rev.*, **126**, 1174–1193.
- Lavaysse, C., A. Diedhiou, H. Laurent, and T. Lebel, 2006: African easterly waves and convective activity in wet and dry sequences of the West African monsoon. *Climate Dyn.*, **27**, 319–332.
- Madden, R., and P. R. Julian, 2005: Historical perspective. *Intraseasonal Variability in the Atmosphere-Ocean Climate System*, W. K. M. Lau and D. E. Waliser, Eds., Springer-Verlag, 436 pp.
- Maloney, E. D., and D. L. Hartmann, 1998: Frictional moisture convergence in a composite lifecycle of the Madden-Julian oscillation. *J. Climate*, **11**, 2387–2403.
- , and —, 2000a: Modulation of eastern north Pacific hurricanes by the Madden-Julian oscillation. *J. Climate*, **13**, 1451–1460.
- , and —, 2000b: Modulation of hurricane activity in the Gulf of Mexico by the Madden-Julian oscillation. *Science*, **287**, 2002–2004.
- , and S. K. Esbensen, 2003: The amplification of east Pacific Madden-Julian oscillation convection and wind anomalies during June–November. *J. Climate*, **16**, 3482–3497.
- , and —, 2007: Satellite and buoy observations of boreal summer intraseasonal variability in the tropical northeast Pacific. *Mon. Wea. Rev.*, **135**, 3–19.
- , D. B. Chelton, and S. K. Esbensen, 2008: Subseasonal SST variability in the tropical eastern North Pacific during boreal summer. *J. Climate*, in press.
- Matthews, A. J., 2000: Propagation mechanisms for the Madden-Julian oscillation. *Quart. J. Roy. Meteor. Soc.*, **126**, 2637–2651.
- , 2004: Intraseasonal variability over tropical Africa during Northern Summer. *J. Climate*, **17**, 2427–2440.
- Mo, K. C., 2000: The association between intraseasonal oscillations and tropical storms in the Atlantic basin. *Mon. Wea. Rev.*, **128**, 4097–4107.
- Mounier, F., and S. Janicot, 2004: Evidence of two independent modes of convection at intraseasonal timescale in the West African summer monsoon. *Geophys. Res. Lett.*, **31**, L16116, doi:10.1029/2004GL020665.
- , —, and G. N. Kiladis, 2008: The West African monsoon dynamics. Part III: The quasi-biweekly zonal dipole. *J. Climate*, **21**, 1911–1928.
- Murakami, T., L.-X. Chen, A. Xie, and M. L. Shresha, 1986: Eastward propagation of 30–60-day perturbations as revealed from outgoing longwave radiation data. *J. Atmos. Sci.*, **43**, 961–971.
- Neelin, J. D., and I. M. Held, 1987: Modeling tropical convergence based on the moist static energy budget. *Mon. Wea. Rev.*, **115**, 3–12.
- Nicholson, S. E., and J. P. Grist, 2003: The seasonal evolution of the atmospheric circulation over West Africa and equatorial Africa. *J. Climate*, **16**, 1013–1030.
- , and Coauthors, 2003: Validation of TRMM and other rainfall estimates with a high-density gauge dataset for West Africa. Part II: Validation of TRMM rainfall products. *J. Appl. Meteor.*, **42**, 1355–1368.
- North, G. R., T. L. Bell, R. F. Cahalan, and F. J. Moeng, 1982: Sampling errors in the estimation of empirical orthogonal functions. *Mon. Wea. Rev.*, **110**, 699–706.
- Redelsperger, J. L., A. Diongue, A. Diedhiou, J. P. Ceron, M. Diop, J. F. Gueremy, and J. P. Lafore, 2002: Multi-scale description of a Sahelian synoptic weather system representative of the West African monsoon. *Quart. J. Roy. Meteor. Soc.*, **128**, 1229–1257.
- , C. D. Thorncroft, A. Diedhiou, T. Lebel, D. J. Parker, and J. Polcher, 2006: African Monsoon Multidisciplinary Analysis: An international research project and field campaign. *Bull. Amer. Meteor. Soc.*, **87**, 1739–1746.
- Reed, R. J., D. C. Norquist, and E. Recker, 1977: The structure and properties of African wave disturbances as observed during Phase III of GATE. *Mon. Wea. Rev.*, **103**, 317–333.
- Riehl, H., 1954: *Tropical Meteorology*. McGraw-Hill, 392 pp.
- Shapiro, L. J., 1987: Month-to-month variability of the Atlantic tropical circulation and its relationship to tropical storm formation. *Mon. Wea. Rev.*, **115**, 2598–2614.
- Sultan, B., and S. Janicot, 2003: The West African monsoon dynamics. Part II: The “preonset” and the “onset” of the summer monsoon. *J. Climate*, **16**, 3407–3427.
- , —, and A. Diedhiou, 2003: The West African monsoon dynamics. Part I: Documentation of intraseasonal variability. *J. Climate*, **16**, 3389–3406.
- Thorncroft, C. D., and B. J. Hoskins, 1994a: An idealized study of African easterly waves. Part I: A linear view. *Quart. J. Roy. Meteor. Soc.*, **120**, 953–982.
- , and —, 1994b: An idealized study of African easterly waves. Part II: A nonlinear view. *Quart. J. Roy. Meteor. Soc.*, **120**, 983–1015.
- , and D. P. Rowell, 1998: Interannual variability of African wave activity in a general circulation model. *Int. J. Climatol.*, **18**, 1305–1323.
- , and K. Hodges, 2001: African easterly wave variability and its relationship to Atlantic tropical cyclone activity. *J. Climate*, **14**, 1166–1179.
- Tomas, R. A., and P. J. Webster, 1997: The role of inertial instability in determining the location and strength of near-equatorial convection. *Quart. J. Roy. Meteor. Soc.*, **123**, 1445–1482.
- Vimont, D. J., and J. P. Kossin, 2007: The Atlantic Meridional Mode and hurricane activity. *Geophys. Res. Lett.*, **34**, L07709, doi:10.1029/2007GL029683.
- Vintzileos, A., and W. M. Thiaw, 2006: On the forecast of cumulative precipitation at subseasonal time-scales over the Sahel. *Geophys. Res. Lett.*, **33**, L14703, doi:10.1029/2006GL026663
- Waliser, D. E., C. Jones, J.-K. E. Schemm, and N. E. Graham,

- 1999: A statistical extended-range tropical forecast model based on the slow evolution of the Madden-Julian oscillation. *J. Climate*, **12**, 1918–1939.
- Wheeler, M., and K. M. Weickmann, 2001: Real-time monitoring and prediction of modes of coherent synoptic to intraseasonal tropical variability. *Mon. Wea. Rev.*, **129**, 2677–2694.
- , and H. H. Hendon, 2004: An all-season real-time multivariate MJO index: Development of an index for monitoring and prediction. *Mon. Wea. Rev.*, **132**, 1917–1932.
- Wu, L., 2007: Impact of Saharan air layer on hurricane peak intensity. *Geophys. Res. Lett.*, **34**, L09802, doi:10.1029/2007GL029564
- Xie, S. P., H. Xu, W. S. Kessler, and M. Nonaka, 2005: Air–sea interaction over the eastern Pacific warm pool: Gap winds, thermocline dome, and atmospheric convection. *J. Climate*, **19**, 5–20.
- Zehr, R. M., 1992: Tropical cyclogenesis in the western North Pacific. NOAA Tech. Rep. NESDIS 61, 181 pp. [Available from U.S. Department of Commerce, NOAA/NESDIS, 5200 Auth Rd., Washington, DC 20233.]